Title
Estimate of Rayleigh-to-Love wave ratio in the secondary microseism by a small array at Piñon Flat observatory, California

Journal
Geophysical Research Letters, 43(21)

ISSN
0094-8276

Authors
Tanimoto, Toshiro
Lin, Chin-Jen
Hadziioannou, Céline
et al.

Publication Date
2016-11-16

DOI
10.1002/2016gl071133

Peer reviewed

Estimate of Rayleigh-to-Love wave ratio in the secondary microseism by a small array at Piñon Flat Observatory, California

Toshiro Tanimoto[1]*, Chin-Jen Lin[2,3], Céline Hadziioannou[3], Heiner Igel[3], and Frank Vernon[4]

1. Department of Earth Science and Earth Research Institute, University of California, Santa Barbara, California 93106, USA.
2. Institute of Earth Sciences, Academia Sinica, Taiwan
3. Department of Earth and Environmental Sciences, Ludwig-Maximilians-University, Theresienstr. 41 80333 Munich, Germany
4. Institute of Geophysics and Planetary Physics, Scripps Institution of Oceanography, La Jolla, California, USA.

*Corresponding author: Email toshiro@geol.ucsb.edu

Abstract

Using closely located seismographs at Piñon Flat (PFO), California, for one-year long record (2015), we estimated the Rayleigh-to-Love wave energy ratio in the secondary microseism (0.1-0.35 Hz) in four seasons. Rayleigh-wave energy was estimated from a vertical component seismograph. Love-wave energy was estimated from rotation seismograms that were derived from a small array at PFO. Derived ratios are 2-2.5, meaning that there is 2-2.5 times more Rayleigh-wave energy than Love-wave energy at PFO. In our previous study at Wettzell, Germany, this ratio was 0.9-1.0, indicating comparable energy between Rayleigh waves and Love waves. This difference suggests that the Rayleigh-to-Love wave ratios in the secondary microseism may differ greatly from region to region. It also implies that an assumption of the diffuse wavefield is not likely to be valid for this low frequency range as the equipartition of energy should make this ratio much closer.

1. Introduction

The cross-correlation Green's function approach was introduced to seismology by Campillo and Paul [2003] and since then, seismic noise has become an indispensable data set for earth structure study. But why this approach works is not necessarily clear. In Campillo and Paul [2003], a diffusive wavefield was assumed for the coda of earthquakes signals in which the equipartition of energy occurred. The equipartition of energy was shown to hold for high-frequency waves (at least higher than 1 Hz), in the coda of seismic phases [Hennino et al., 2001; Margerin et al., 2009] but the main frequency range that we have benefitted by the cross-correlation approach has been the microseism frequency band (0.05-0.4 Hz). For such a low frequency range, Snieder [2004] argued that the equipartition of energy is not likely to occur and presented a ballistic wave concept. We tend to agree with his view for the microseism frequency range but our fundamental problem is the lack of understanding on the nature of seismic noise.

In this paper, we attempt to find out the relative amount of Love waves with respect to Rayleigh waves in seismic noise in the microseism frequency band. In our previous papers [Tanimoto et al., 2015, 2016], we took advantage of a unique set of instruments at Wettzell (WET), Germany, where an STS-2 seismograph and a ring laser [Schreiber et al., 2009; Schreiber and Wells, 2013] are co-located. Since the ring laser at WET records the vertical component of rotation in contrast to strain or translational components at Earth's surface, they are only sensitive to Love waves (for a plane-layered structure). Combined with a vertical-component seismometer, which mainly records Rayleigh waves, we made estimates for the energy ratio between Rayleigh waves and Love waves.

In this paper, instead of using the ring laser data, we retrieve the rotation from closely located broadband instruments at Piñon Flat [Lin et al., 2016], California, by following an approach by Spudich et al. [1995] and Spudich and Fletcher [2008, 2009]. This dense array has been in operation since 2014. We use this data set for the entire 2015 to estimate the Rayleigh-to-Love wave energy ratios at PFO. We find that the Rayleigh-to-Love wave energy ratio is about 2-2.5, which is quite different from our results at Wettzell (0.9-1.0). Rayleigh waves seem dominant in the secondary microseism at PFO. We also point out that this large difference between WET and PFO is inconsistent with the assumption of diffuse wavefield for the microseism frequency band.

We describe our data in section 2, surface accelerations between Rayleigh and Love waves in section 3 and their energy ratios in section 4. We briefly discuss the implications of our results in section 5.

2. Data

Since late in 2014, there have been thirteen broadband seismographs installed at PFO as a small array. Fig. 1a shows two maps to indicate the location of PFO and detailed locations of broadband seismic stations at PFO in addition to the ring laser (yellow) and three strain meters (pink lines). Broadband stations are indicated by green, blue, and red circles. Lin et al. [2016] has done a comparison study between the ring laser rotation data (yellow) and the rotation that can be derived by differencing various pairs of seismograms [Spudich and Fletcher, 2008, 2009]. A general conclusion by Lin et al. [2016] is that the rotation is best derived by using the large array, indicated by green circles in Fig. 1a. Even so, there are slight differences in Love-wave amplitudes between the array-derived amplitudes and the ring-laser rotation amplitudes. But as long as waveform cross-correlation is larger than 0.94, amplitude differences are less than 4.5 percent. This level of difference does not affect our conclusion in this paper.

Out of thirteen stations, BPH03 is explicitly marked in this figure because we analyzed the rotation for this location for the estimate of Love-wave energy. We used vertical component seismograms at this location to estimate Rayleigh-wave energy. The ring laser data (at the yellow square) were not used because the instrument was not sensitive enough to record microseisms. We present our analysis for one-year long data in 2015, separately analyzed for four seasons.

The approach in this paper is similar to the one in our previous studies [Tanimoto et al., 2015; 2016] except for minor details. In this study, we analyzed every 1-hour record in 2015, first computing the power spectral density (PSD) for all 1-hour records and eliminating time portions that were obviously influenced by large earthquakes and data gaps. Then we used two earthquake catalogues to reduce earthquake effects further; one was the Global Moment Tensor catalogue [Dziewonski et al., 1983; Ekström et al., 2012] that allowed us to remove global earthquake effects with magnitude 5.5 and larger. The other was the SCSN Moment tensor catalogue [SCEDC, 2013] that allowed us to remove regional (Southern California) earthquake effects with magnitude 3.0 and larger in 2015. For large earthquakes ($M>5.5$) we removed six hours after the origin time and for small earthquakes ($M>3.0$), we removed two hours from their origin times. This processing is important because large earthquakes generated large-amplitude body and surface waves near 0.1 Hz.

We then binned data into four seasons; Winter data are from January, February and December, Spring data from March, April and May, Summer data from July and

August and Fall data from September, October and November. Then for the identified "earthquake-free" 1-hour portions in 2015, we computed Fourier spectra and averaged Fourier amplitudes for each season. Fig. 1b shows the average vertical-component spectral amplitudes for each season as a function of frequency; blue is Winter, green is Spring, red is Summer and yellow is Fall. Fig. 1c shows the averaged spectral amplitudes for the rotation data. In both plots, instead of using the power spectral density, we show the averaged $\sqrt{|F(\omega)|^2 / T}$ where $F(\omega)$ is the Fourier spectra and T is the length of time series (1 hour). We used Fourier amplitudes rather than PSD because we want to estimate surface amplitudes of Rayleigh and Love waves that are linearly proportional to spectral amplitudes.

For both vertical-component (Fig. 1b) and rotational spectra (Fig. 1c), amplitudes in winter (blue) are the largest and the peak frequency (~ 0.15 Hz) becomes the lowest frequency among the four seasons. Amplitudes in summer (red) are the smallest among the four seasons and their peak frequency becomes higher (~ 0.2 Hz). Amplitudes in spring and fall are between these two end-member seasons. These features are typical seasonal characteristics found for stations in the northern hemisphere. The main point here is that the effects from earthquakes seem to be removed successfully from these spectra as earthquakes could disturb the clean background seasonal variations in seismic noise.

For frequencies below 0.1 Hz, amplitudes show large differences between vertical-component spectra (Fig. 1b) and the rotational spectra (Fig. 1c). In Fig. 1b, we can see a small peak at about 0.05-0.07 Hz, which is the well-known primary microseism peak (the same frequency with ocean waves). However, we cannot see this peak in the rotation spectra (Fig. 1c). Instead, we see a large peak at about 0.01-0.02 Hz. In fact, rotational spectral amplitudes seem to increase toward lower frequencies even further. We suppose that large tilt-related noise in horizontal component seismograms, which increases toward lower frequencies, might be the reason for this trend but the exact cause is not known for the moment. Fig. 1c shows a trend that goes to zero because we detrend data in the analyses and kept the zero-frequency data in this plot. For positive-frequency data the spectral amplitudes keep increasing toward lower frequencies. It seems clear that this large low-frequency noise is masking the primary microseism peak near 0.05-0.07 Hz. Based on this observation, we report only on the results of secondary microseism in this paper.

3. Acceleration spectra

The rotational spectral amplitudes in Fig. 1c can be converted to surface transverse acceleration if twice the Love-wave phase velocity (2C) is multiplied to the spectra [Pancha et al., 2000]. In this study, we examined three seismic velocity models for PFO and used their Love-wave phase velocities to obtain transverse spectral amplitudes. The three models are (i) SCEC CVM (Southern California Earthquake Center Community Velocity Model, Shaw et al., 2015), (ii) 1-D model based on tomographic results derived from the ANZA network data [Scott et al., 1994] where PFO is included, and (iii) a local structure at PFO based on the receiver function analysis [Baker et al., 1996]. P-wave and S-wave velocity in the upper 30 km are shown in the top panel of Fig. 2 and their Love-wave dispersion curves are shown in the bottom panel. In these figures, SCEC CVM is the SCEC model, Anza refers to the structure by Scott et al. [1994] and RF refers to the receiver function results by Baker et al. [1996]. The first two models

(SCEC and Anza) have similar Love-wave phase velocity but the third one (RF) has Love-wave phase velocity that is about 10 percent slower. Since we multiply 2C (twice the Love-wave phase velocity) to the rotational spectra in Fig. 1(c) to obtain the transverse spectra [Pancha et al., 2000; Igel et al., 2005, 2007; Ferreira and Igel, 2009; Hadziioannou et al., 2012], these differences in phase velocity lead to about 10 percent differences in the transverse acceleration.

Fig. 3 shows four acceleration spectra, the transverse acceleration spectra (red) from the rotation time series and the vertical (Z, blue), the north-south (NS, green) and the east-west (EW, black) acceleration spectra obtained from seismograms at BPH03. Since three models give similar results, only the results for the SCEC model are shown in Fig. 3. Four panels correspond to the results in Winter (a), Spring (b), Summer (c) and Fall (d).

In all seasons, two horizontal accelerations (NS and EW) are slightly higher than transverse acceleration but they all have similar frequency dependence. Differences in amplitudes about 0.15 Hz among NS, EW and transverse spectra may be explained by the effects of Rayleigh waves. The maximum peak frequencies change according to season but all four acceleration spectra basically have the same peak frequencies in each season.

Love-wave phase velocity for the third seismic model (RF) is about 10 percent slower than two other models and it causes 10 percent reduction of transverse accelerations. But spectral shape of transverse acceleration remains quite similar. This amplitude difference leads to smaller estimates of transverse acceleration and Love-wave energy by 10 percent.

4. Energy ratios between Rayleigh waves and Love waves

Results in Fig. 3 give us information on surface amplitudes of Rayleigh waves and Love waves. Essentially we get the surface values of Rayleigh-wave eigenfunctions (U and V) and Love-wave eigenfunction (W) from them [Tanimoto et al., 2016]. Since the energy of surface waves are given by the depth integrals as $E_R = \omega^2 \int \rho\{U(z)^2 + V(z)^2\} dz$ and $E_L = \omega^2 \int \rho W(z)^2 dz$, where E_R and E_L are Rayleigh- and Love-wave energy, we can evaluate them without any difficulty for three seismic models.

Figures 4b, 4c and 4d show the Rayleigh-to-Love wave energy ratios (R/L) for frequencies between 0.10 and 0.35 Hz. Each season is denoted by a different color. The maximum ratios are found at about 0.20 Hz in summer and the ratios are about 4. In other seasons, the ratios are about 2.0-3.0. The energy ratios become lower for frequencies close to 0.1 Hz.

The average ratios between 0.10 and 0.35 Hz in each season are shown in Fig. 4a. In this panel, three colors indicate three seismic models. All ratios fall within the range 2.0-2.5, meaning that the Rayleigh wave energy is about 2-2.5 times larger than the Love-wave energy. But this is the overall average. It should be kept in mind that this ratio can be as high as 4.0 in summer near its peak frequency (0.20 Hz) and about 3.0 in other seasons near their peak frequencies (0.15 Hz).

There is a hint for higher R/L ratios in spring and summer in Fig. 4a, but it does not stand the statistical test as error bars indicate. But we note this tendency of higher summer R/L ratio is consistent with what Tanimoto et al. [2016] reported for the Wettzell study.

5. Discussion

The main result in this paper is the average R/L energy ratio of 2.0-2.5 at PFO. Depending on the seismic velocity models, there are some variations but the estimated ratios fall in this relatively small range. This relative dominance of Rayleigh waves may have been the reason that Schulte-Pelkum et al. [2004] observed clean and azimuthally stable Rayleigh-wave arrivals from the ANZA array analysis.

In our analysis for Wettzell (Germany) data, we obtained the R/L ratio of about 0.9-1.0. This value means that the Love-wave energy and the Rayleigh-wave energy are comparable. There are some uncertainties in those energy estimates that can arise from a choice of seismic velocity structure, but this difference in the R/L ratio by a factor of two is significant. It seems safe to state that the R/L energy ratios are substantially different between Wettzell and Piñon Flat.

This large difference in R/L ratio suggests that the assumption of diffuse wavefield fails for the microseism frequency range. The equipartition of energy should occur in a diffuse wavefield [e.g., Weaver, 2010] and if so, R/L ratios should not vary very much from region to region. It is not easy to test the validity of this assumption, however, because mode shapes are different depending on earth structure but one would not expect a large difference in the R/L ratios. Many seismic noise analyses for earth structure were conducted by assuming the diffuse wavefield, including the noise cross-correlation Green's function analysis [Campillo and Paul, 2003] and H/V analysis [e.g. Sanchez-Sesma et al., 2011]. We should stress, however, that the latter H/V analysis was done in higher frequency ranges than the microseism frequency range. The assumption of the diffuse wavefield was shown to work for higher frequencies, for example between 5 and 7 Hz [Margerin et al., 2009], in the coda of large-amplitude seismic phases. The result of this study only indicates that it does not hold in the microseism frequency range.

If a propagation path is long, the wavefield could become closer to a diffusive field even for the microseism frequency range, because for a long propagation path, there will be more chances of scattering and wave conversion. Comparable energy between Rayleigh waves and Love waves at WET may be related to this case as Wettzell is quite far from the coasts in all azimuths. On the other hand, since PFO is relatively close to the California coast, the propagation distance may be too short to create a diffusive wavefield for the microseism frequency range.

There are a few other recent studies that have estimated the energy ratios between Rayleigh and Love waves. Nishida et al. [2008] reported results in Japan and their ratio estimate for the secondary microseism of about 2 is close to our estimate for PFO. Juretzek and Hadziioannou [2016] obtained ratios from multiple array analyses in Europe and their results range between 0.8 and 2.5, depending on location and season. Our result for PFO is similar to Japanese results and is near the upper end of Juretzek and Hadziioannou [2016], although the latter study reported a somewhat large range of ratios. The lowest end of their estimate is consistent with our result for Wettzell. But we should be careful in those comparisons because even in our current results, the ratio can reach 4 in summer for the peak frequency range (0.19-0.20 Hz) and 3 in other seasons for their peak frequency ranges of about 0.15 Hz. The total average for the range 0.10-0.35 Hz may be 2.0-2.5, there are quite large variations with respect to frequencies and seasons.

Our results also indicate a need for better understanding of the Love-wave excitation sources, especially their power and the mechanisms of their excitation.

Compared with our understanding of Rayleigh-wave excitation in the secondary microseism [Longuet-Higgins, 1950], our understanding of Love-wave excitation in the secondary microseism is still quite vague. It appears that we can form two hypotheses; one is a conversion hypothesis. Ocean wave collisions (the Longuet-Higgins mechanism) can create double-frequency Rayleigh waves in deep oceans. As these Rayleigh waves propagate toward seismic stations on land, a fraction of them may convert to Love waves at a sharp ocean-continent boundary. Numerical simulations (e.g., Ying et al, 2014; Gualtieri et al., 2013, 2015) are clearly needed to understand the importance of this propagation effect. The other hypothesis is that the double-frequency ocean waves that are generated by collision of ocean waves, reach shallow oceans near the coast and interact with the solid earth directly [e.g., Saito, 2010]. Both mechanisms may contribute to Love-wave excitation and regional variations in the R/L ratios may be explained by a combination of these effects. But we need more careful analysis in the future.

Acknowledgments

All data used in this study, the thirteen broadband seismic data at PFO, can be obtained from the IRIS data center in Seattle, Washington, USA. TT acknowledges support from NSF-EAR 1547523, HI from the ERC Advanced Grant "ROMY", CH from grant HA7019/1-1 by the Emmy-Noether Programme of the German Research Foundation (DFG).

References

Baker, G. Eli, J. B. Minster, G. Zandt, and H. Gurrola (1996), Constraints on crustal structure and complex Moho topography beneath Pinon Flat, California, from teleseismic receiver functions, Bull. Seism. Soc. Am., 86, 1830-1844.

Campillo, M. and A. Paul, (2003). Long range correlations in the diffuse seismic coda, Science, 299, 547-549.

Dziewonski, A. M., T.-A. Chou and J. H. Woodhouse (1981), Determination of earthquake source parameters from waveform data for studies of global and regional seismicity, J. Geophys. Res., 86, 2825-2852. doi:10.1029/JB086iB04p02825

Ekström, G., M. Nettles, and A. M. Dziewonski (2012), The global CMT project 2004-2010: Centroid-moment tensors for 13,017 earthquakes, Phys. Earth Planet. Inter., 200-201, 1-9. doi:10.1016/j.pepi.2012.04.002

Ferreira, A. and I. Igel (2009), Rotational motions of seismic surface waves in a laterally heterogeneous Earth, Bull. Seism. Soc. Am., 99(2B), 1429-1436.

Gualtieri, L., E. Stutzmann, Y. Capdeville, F. Ardhuin, M. Schimmel, A. Mangeney and A. Morelli (2013). Modelling secondary microseismic noise by normal mode summation, Geophys. J. Int., 193, 1732-1745, doi:10.1093/gji/ggt090.

Gualtieri, L., E. Stutzmann, Y. Capdeville, V. Farra, A. Mangeney, and A. Morell(2015), On the shaping factors of the secondary microseismic wavefield, *J. Geophys. Res. Solid Earth*, *120*, 6241–6262, doi:10.1002/2015JB012157.

Hadziioannou, C., P. Gaebler, U. Schreiber, J. Wassermann, and H. Igel (2012), Examining ambient noise using co-located measurements of rotational and translational motion, *J. Seismol*., **16**, 787, doi:10.1007/s10950-012-9288-5.

Hennino, R., Tregoures, N., Shapiro, N.M., Margerin, L., Campillo, M., van Tiggelen, B.A. & Weaver, R.L., 2001. Observation of equipartition of seismic waves, Phys. Rev. Lett., 86, 3447–3450, DOI: 10.1103/PhysRevLett.86.3447

Igel, H., U. Schreiber, A. Flaws, B. Schuberth, A. Velikoseltsev, and A. Cochard (2005), Rotational motions induced by the M8.1 Tokachioki earthquake, September 25, 2003, *Geophys. Res. Lett.,* 32, L08309, doi:10.1029/2004GL022336.

Igel H, Cochard A, Wassermann J, Flaws A, Schreiber U, Velikoseltsev A, Pham Dinh N (2007) Broad-band observations of earthquake-induced rotational ground motions, *Geophys. J Int.,* 168(1):182–196

Juretzek, C. and C. Hadziioannou (2016), Where do ocean microseisms come from? A study of Love-to-Rayleigh wave ratios, J. Geophys. Res., Solid Earth, 121, doi:10.1002/2016JB013017.

Lin, Chin-Jen, F. Vernon, J. Wassermann, A. Gebauer, U. Schreiber, S. Donner, C. Hadziioannou, D. Agnew, and Heiner Igel (2016), Comparison of Direct and Array-derived strain and rotation at the Piñon Flat Observatory, California, EGU General Assembly, 18, 7753.

Longuet-Higgins, M. (1950), A theory of the origin of microseisms. *Phil. Trans. R. Soc. Lond., Ser A*, *Math. Phy.s Sci.,* 243(857), 1–35.

Margerin, L., M. Campillo, B. A. Van Tiggelen, and R. Hennino (2009). Energy partition of seismic coda waves in layered media: theory and application to Pinyon Flats Observatory, Geophys. J. Int., 177, 571-585, doi: 10.1111/j.1365-246X.2008.04068.x

Nishida K, Kawakatsu H, Fukao Y, Obara K (2008) Background Love and Rayleigh waves simultaneously generated at the Pacific Ocean floors, *Geophys. Res. Lett.,* 35(16):1–5

Pancha A., T.H. Webb, G. E. Stedman,D. P. McLeod, and K. U. Schreiber (2000), Ring laser detection of rotations from teleseismic waves, *Geophys Res Lett* 27(21):3553

Saito, T., (2010), Love-wave excitation due to the interaction between a propagating ocean wave and the sea-bottom topography, Geophys. J. Int., 182, 1515-1523, doi:10.1111/j.1365-246X.2010.04695.x

SCEDC (2013): Southern California Earthquake Center. Caltech.Dataset. doi:10.7909/C3WD3xH1

Schreiber, U., and J.-P. Wells (2013), Invited Review Article: Large ring laser for rotation sensing, *Rev. Sci. Instrum*., 84, 041101, doi:10.1063/1.4798216.

Schreiber, U., J. N. Hautmann, A. Velikoseltsev, J. Wassermann, H. Igel, J. Otero, F. Vernon, and J.‐P. R. Wells (2009b), Ring laser measurements of ground rotations for seismology, *Bull. Seism. Soc. Am.,* 99(2B), 1190–1198, doi:10.1785/0120080171

Schulte-Pelkum, V., P. S. Earle, and F. Vernon (2004). Strong directivity of ocean-generated seismic noise, G-cubed, 5, Q03004, doi:10.1029/2003GC000520

Scott, J., T. G. Masters, and F. L. Vernon (1994). 3-D velocity structure of the San Jacinto Fault zone near Anza, California, Geophys. J. Int., 119, 611-626.

Shaw, J., A. Plesch, C. Tape, M.P. Suess, T. H.Jordan, G. Ely, E. Hauksson, J. Tromp, T. Tanimoto, R. Graves, K. Olsen, C. Nicholson, P. J.Maechling, C. Rivero, P. Lovely, C. M. Brankman, J. Munster (2015). Unified Structural Representation of the southern California crust and upper mantle, Earth Planet. Sci. Lett., 415, 1-15. doi: 10.1016/j.epsl.2015.01.016

Snieder, R. (2004). Extracting the Green's function from the correlation of coda waves:

A derivation based on stationary phase, Phys. Rev. E, 69, 046610, DOI:10.1103/PhysRevE.69.046610

Spudich, P. and J. B. Fletcher (2008). Observation and prediction of dynamic ground strains, tilts, and torsions caused by the M 6.0 2004 Parkfield, California, earthquake and aftershocks derived from UPSAR array observations, Bull. Seism. Soc. Am., 98, 1898-1914, doi:10.1785/0120070157.

Spudich, P. and J. B. Fletcher (2009). Software for inference of dynamic ground strains and rotations and their errors from short baseline array observations of ground motions, Bull. Seism. Soc. Am., 99, 1480-1482, doi:10.1785/0120080230

Spudich, P., L. K. Steck, M. Hellweg, J. Fletcher, and L. M. Baker (1995). Transient stresses at Parkfield, California, produced by the M 7.4 Landers earthquake of June 28, 1992: observations from the UPSAR dense seismograph array, *J. Geophys. Res*., 100, 675-690.

Tanimoto, T., C. Hadziioannou, H. Igel, J. Wasserman, U. Schreiber, and A. Gebauer (2015), Estimate of Rayleigh-to-Love wave ratio in the secondary microseism by colocated ring laser and seismograph, Geophys. Res. Lett., 42, doi:10.1002/2015GL063637.

Tanimoto, T., C. Hadziioannou, H. Igel, J. Wassermann, U. Schreiber, A. Gebauer, and

B. Chow (2016), Seasonal variations in the Rayleigh-to-Love wave ratio in the secondary microseism from colocated ring laser and seismograph, J. Geophys. Res. Solid Earth, 121, 2447–2459, doi:10.1002/2016JB012885.

Weaver, R.L., 2010. Equipartition and retrieval of Green's function. Earthquake Science, 23(5), pp.397-402.

Ying, Y., C. J. Bean, and P. D. Bromirski (2014), Propagation of microseisms from the deep ocean to land, Geophys. Res. Lett., *41*,6374–6379, doi:10.1002/2014GL060979.

Figure Captions

Fig. 1. **(a)** Two maps on the left indicate the location of PFO. Locations of thirteen broadband seismographs at PFO are shown on the right (red, blue and green circles). We analyzed rotation, derived from the green stations. BPH03 is the location around which rotation was derived from this array. RLG is the ring laser gyroscope and three lines indicate the locations of strain meters. **(b)** Fourier amplitudes of vertical acceleration at BPH03 in four seasons. **(c)** Fourier amplitudes of rotation rate in four seasons. Earthquake effects were removed from (b) and (c) by using two catalogues.

Fig. 2: **(a)** P-wave and S-wave velocity structure for three seismic models. Models are SCEC CVM, 1-D structure from a tomographic study [Scott et al., 1994] and structure from a receiver function study at PFO [Baker et al., 1996]. **(b)** Love-wave fundamental-mode phase velocity for the three models. They were used to transform rotation rate to transverse acceleration.

Fig. 3: Acceleration spectra at BPH03. Z (blue), N (green) and E (black) are vertical, NS and EW acceleration spectra from seismometer at BPH03. Transverse acceleration (red) was obtained from the rotation spectra by multiplying 2C where C is Love-wave phase velocity (Fig. 2b). Results for (a) winter, (b) spring, (c) summer and (d) fall.

Fig. 4: **(a)** Rayleigh-to-Love wave energy (R/L) ratios in four seasons. The results for three seismic velocity models are shown in different colors. They are averaged ratios for frequencies between 0.1 and 0.35 Hz. (b) R/L ratios when the SCEC CVM model was used. Different colors are for different seasons. (c) Same with (b) except that the Anza model was used. (d) Same with (b) except that the RF model was used.

Figure 1.

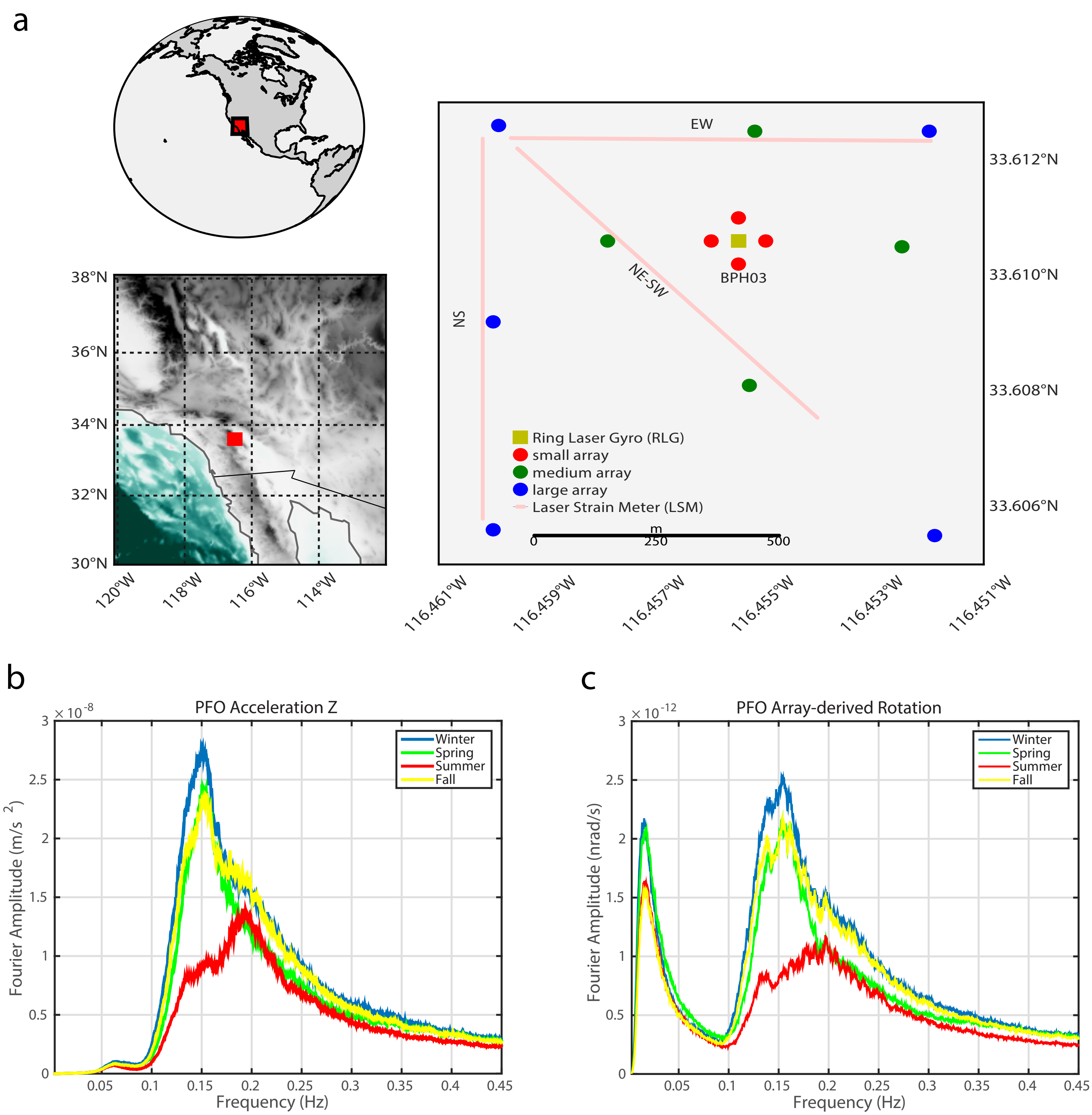
a
38°N
36°N
34°N
32°N
30°N
120°W
118°W
116°W
114°W
EW
NS
NE-SW
BPH03
33.612°N
33.610°N
33.608°N
33.606°N
Ring Laser Gyro (RLG)
small array
medium array
large array
Laser Strain Meter (LSM)
m
0
250
500
116.461°W
116.459°W
116.457°W
116.455°W
116.453°W
116.451°W
b
PFO Acceleration Z
× 10^-8
Fourier Amplitude (m/s^2)
Frequency (Hz)
Winter
Spring
Summer
Fall
c
PFO Array-derived Rotation
× 10^-12
Fourier Amplitude (nrad/s)
Frequency (Hz)
Winter
Spring
Summer
Fall

Figure 2.

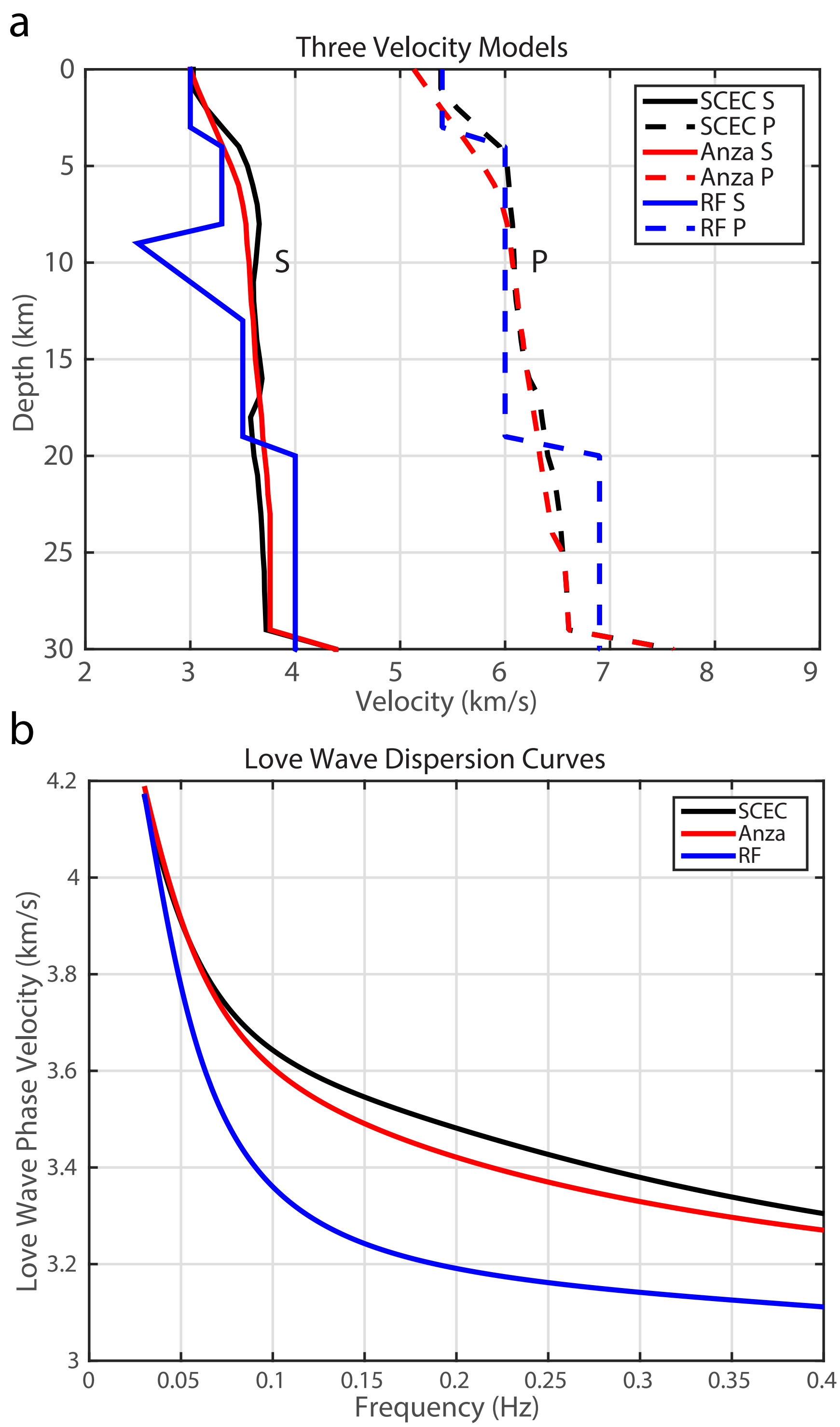
a
Three Velocity Models
Depth (km)
Velocity (km/s)
S
P
SCEC S
SCEC P
Anza S
Anza P
RF S
RF P
0
5
10
15
20
25
30
2
3
4
5
6
7
8
9
b
Love Wave Dispersion Curves
Love Wave Phase Velocity (km/s)
Frequency (Hz)
SCEC
Anza
RF
4.2
4
3.8
3.6
3.4
3.2
3
0
0.05
0.1
0.15
0.2
0.25
0.3
0.35
0.4

Figure 2

Figure 3.

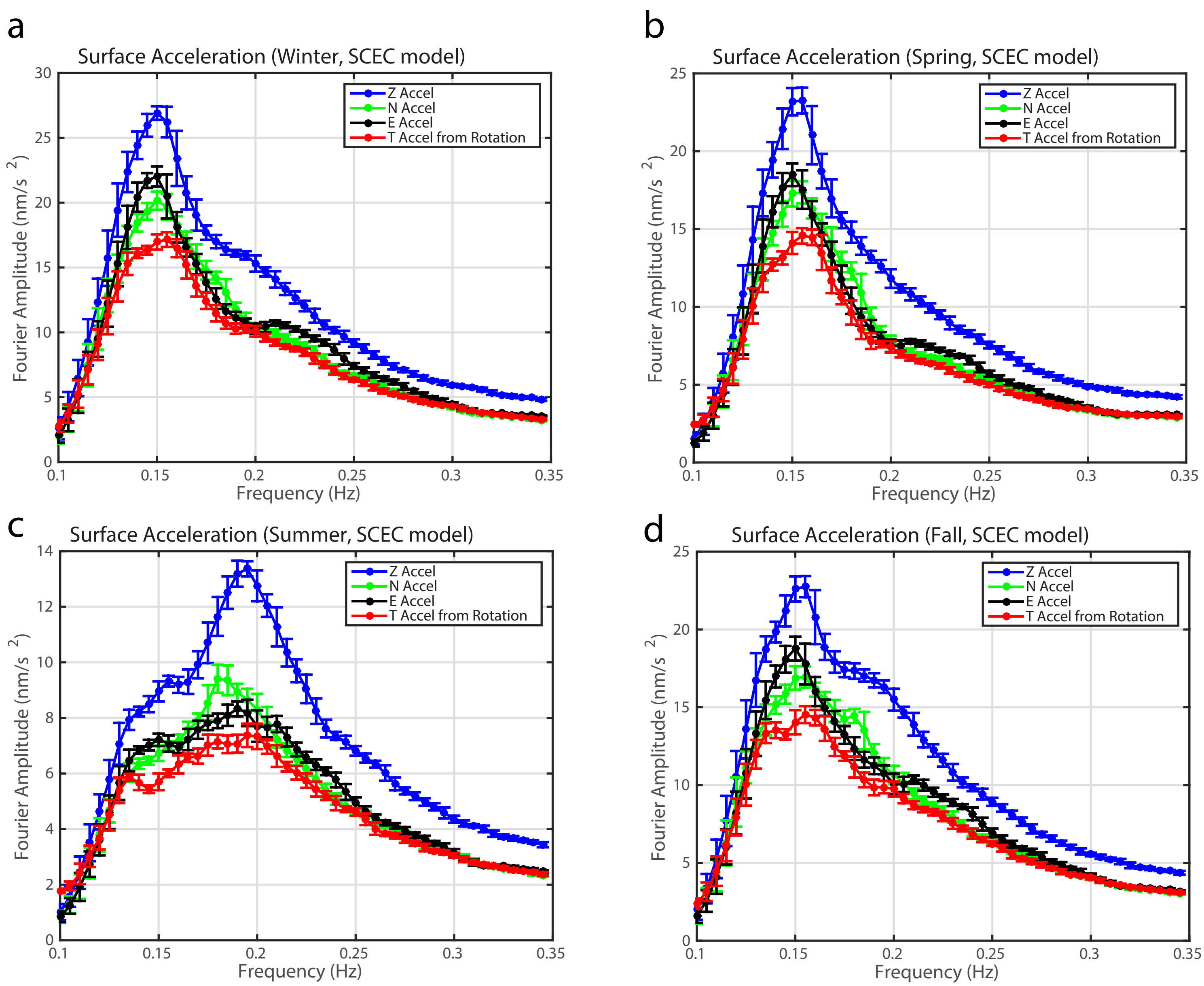
a
Surface Acceleration (Winter, SCEC model)
b
Surface Acceleration (Spring, SCEC model)
c
Surface Acceleration (Summer, SCEC model)
d
Surface Acceleration (Fall, SCEC model)
Z Accel
N Accel
E Accel
T Accel from Rotation
Fourier Amplitude (nm/s 2)
Frequency (Hz)

Figure 3

Figure 4.

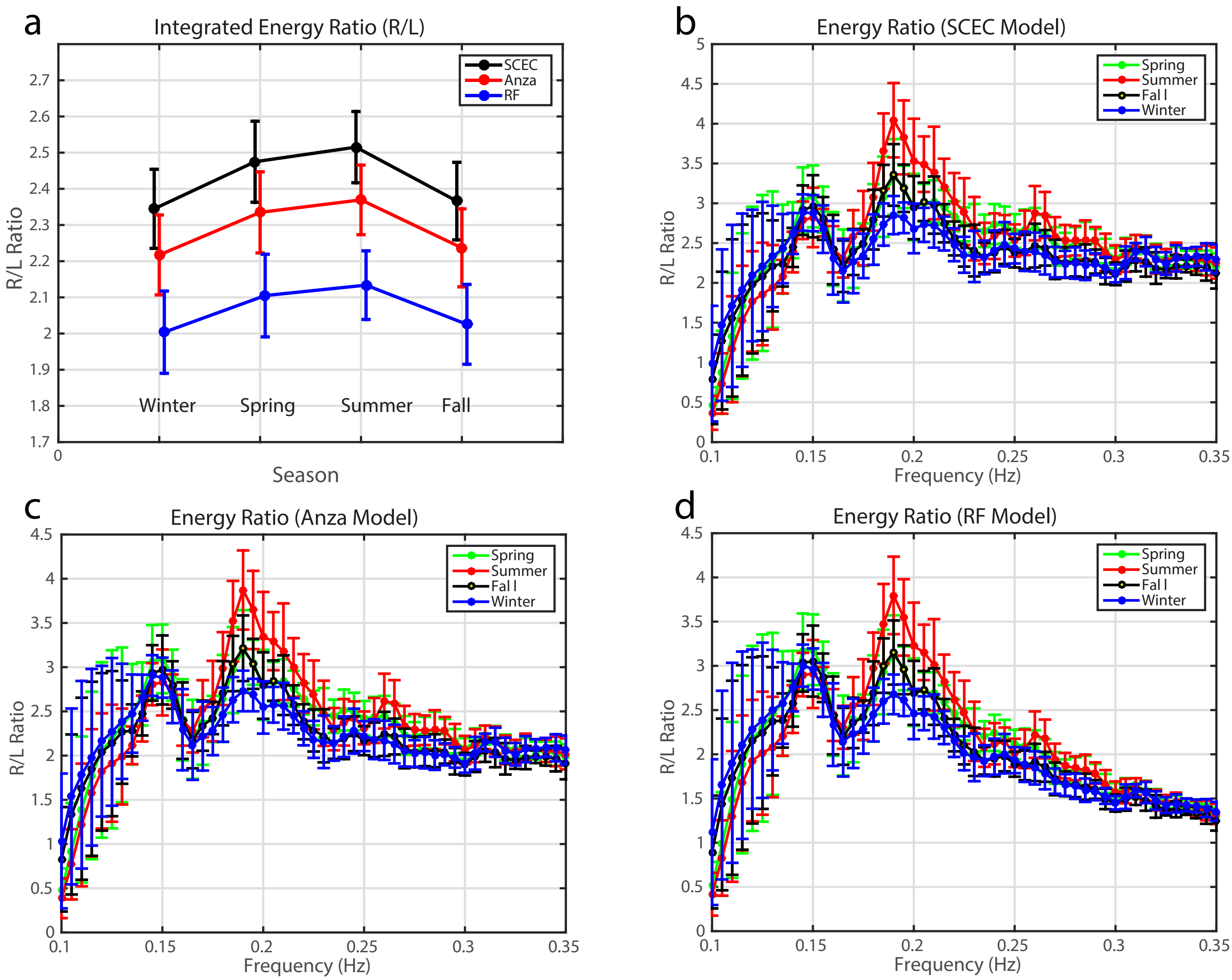
a
Integrated Energy Ratio (R/L)
SCEC
Anza
RF
R/L Ratio
Winter
Spring
Summer
Fall
Season
b
Energy Ratio (SCEC Model)
Spring
Summer
Fal l
Winter
R/L Ratio
Frequency (Hz)
c
Energy Ratio (Anza Model)
Spring
Summer
Fal l
Winter
R/L Ratio
Frequency (Hz)
d
Energy Ratio (RF Model)
Spring
Summer
Fal l
Winter
R/L Ratio
Frequency (Hz)

Figure 4